Journal of Energy Storage 132 (2025) 117984

Contents lists available at ScienceDirect

Journal of Energy Storage

journal homepage: www.elsevier.com/locate/est

Research papers

In situ construction of Fe_2MoC nanostructures on VNbC MXene carbon nanofibers for enhanced lithium-ion battery performance

Xiaohong Lu [a], Yinghui Wang [a,*], Weili Chen [a], Wan Chang [a,*], Deyang Zhang [b], Kangwen Qiu [c], Paul K. Chu [d], Hailong Yan [a], Jinbing Cheng [a,*]

[a] Henan International Joint Laboratory of MXene Materials Microstructure, College of Physics and Electronic Engineering, Nanyang Normal University, Nanyang 473061, China
[b] Key Laboratory of Microelectronics and Energy of Henan Province, Xinyang Normal University, Xinyang 464000, China
[c] College of Energy Engineering, Huanghuai University, Zhumadian 463000, China
[d] Department of Physics, Department of Materials Science & Engineering, and Department of Biomedical Engineering, City University of Hong Kong, Tat Chee Avenue, Kowloon, Hong Kong, China

ARTICLE INFO

Keywords:
MXene
Fe_2MoC
Electrospinning
Lithium-ion battery
Carbon nanofiber

ABSTRACT

The performance of lithium-ion battery (LIB) electrodes is often constrained by limited rate capability and poor cycling stability, primarily due to sluggish ion transport and structural degradation. To overcome these limitations, we engineered uniform Fe_2MoC nanostructures onto VNbC MXene-based hollow multichannel carbon fibers (HMCFs) using a synergistic combination of coaxial electrospinning and hydrothermal synthesis. The interfacial self-assembly process promotes the formation of a stable Fe_2MoC layer, which significantly enhances both electronic and ionic conductivity. Meanwhile, the hollow fiber architecture effectively accommodates volume changes during electrochemical cycling, thereby improving mechanical integrity and stability. In situ XRD analysis was employed to elucidate the lithium storage mechanism of the Fe_2MoC@VNbC/HMCFs composite electrode, confirming its robust structural evolution during charge-discharge cycles. Electrochemical testing revealed an impressive average discharge capacity of 800.8 mAh g^{-1}, representing a 41 % enhancement compared to its VNbC/HMCF counterpart. Moreover, the composite electrode demonstrated excellent rate performance and long-term cycling stability under both symmetric and full-cell configurations. These results highlight the potential of Fe_2MoC@VNbC/HMCFs as a high-performance anode material for next-generation lithium-ion batteries, driven by its optimised one-dimensional nanostructure and dual-metal MXene integration.

1. Introduction

The rapid advancement of electric vehicles and portable electronic devices has driven a growing demand for lithium-ion batteries (LIBs) with higher energy and power densities, as well as rapid charging capabilities [1]. Conventional commercial electrodes, such as graphite and lithium titanate, suffer from limited theoretical capacities and slow redox kinetics, which hinder their performance. To address these limitations, various alternative electrode materials with improved power density and extended cycle life have been developed [2]. For instance, two-dimensional materials such as MXenes and transition metal carbides (TMCs) have been proposed as promising candidates due to their high capacity and excellent electrical conductivity. However, in lithium-ion battery electrodes, issues such as capacity degradation from self-stacking and volume expansion during lithiation/delithiation significantly hinder their cycling stability and rate performance. Recently, numerous strategies have been explored to improve the electrochemical performance of MXenes and TMCs, with particular emphasis on nanostructure engineering and their integration with carbonaceous materials such as graphene, carbon nanotubes, and carbon nanofibers [3]. These engineered structures not only offer ample internal space to accommodate volume changes during cycling but also introduce abundant interfacial sites that facilitate enhanced ion transport.

Various carbonaceous materials have been integrated with TMCs to construct fast ion and electron conduction networks. Compared to conventional carbon substrates, two-dimensional MXenes offer larger interlayer spacings and abundant surface functional groups, which serve as active sites for Li^+ adsorption and contribute to enhanced lithium

* Corresponding authors.
E-mail addresses: yhsewang@163.com (Y. Wang), changwan@nynu.edu.cn (W. Chang), chengjinbing1988@163.com (J. Cheng).

https://doi.org/10.1016/j.est.2025.117984
Received 5 May 2025; Received in revised form 8 July 2025; Accepted 2 August 2025
Available online 8 August 2025
2352-152X/

storage performance. In addition, MXenes possess a unique layered structure, excellent electrical conductivity, and strong chemical stability [4]. However, their practical energy storage performance remains limited, as the nanosheets tend to restack due to hydrogen bonding and van der Waals interactions, leading to reduced active surface area and restricted electrolyte accessibility [5]. Furthermore, MXene is susceptible to oxidation and structural degradation, making it necessary to inhibit both restacking and oxidative instability. These challenges can be effectively addressed through rational nanostructure design and the incorporation of MXene nanosheets into carbon nanofiber matrices. The confinement effect and protective function of carbon nanofibers effectively inhibit MXene self-stacking and oxidation, thereby preserving structural integrity and enhancing electrochemical stability. Meanwhile, electrospinning enables the fabrication of layered one-dimensional nanofibers that enlarge the electrode and electrolyte interface, promote strain relaxation, lower ion diffusion barriers, and improve overall structural stability [6]. MXene-based composites have demonstrated significant potential for industrial applications owing to their superior electrochemical properties and structural versatility [7].

In this study, hollow multichannel carbon fibers (VNbC/HMCFs) are integrated with conductive $VNbCT_x$ MXene substrates to develop electrode materials with enhanced energy densities. A straightforward hydrothermal approach is employed for the in situ synthesis of bimetallic Fe_2MoC nanoparticles on the substrate, ensuring structural integrity while promoting the formation of robust interfacial bonding. This novel strategy effectively reduces the aggregation and migration of Fe_2MoC nanoparticles, issues that would otherwise compromise rate capability and cycling stability. The hydrothermally synthesized Fe_2MoC composite integrated with VNbC hollow multichannel carbon fibers (Fe_2MoC@VNbC/HMCFs) exhibits an average discharge specific capacity of 800.8 mAh g^{-1}, reflecting a 41 % improvement over the unmodified counterpart. The hollow carbon nanofibers effectively buffer volume change during lithium insertion and extraction, thereby contributing to excellent cycling stability. Even after 600 cycles at a high current density of 2 A g^{-1}, the electrode retains a capacity of 471.6 mAh g^{-1}. The full cell assembled with this electrode demonstrates a capacity retention of 72.5 % after 400 cycles at a current density of 0.1 A g^{-1}, highlighting the effectiveness of bimetallic carbides such as Fe_2MoC in enhancing the performance of lithium-ion batteries. Moreover, the in situ self-assembly strategy combined with rational nanostructure design offers valuable insights for the development of high-performance electrode materials for lithium-ion batteries.

2. Results and discussion

As illustrated in Fig. 1, a few-layer $VNbCT_x$ MXene is synthesized via selective etching and exfoliation of the VNbAlC MAX phase. Electrospinning is utilized to fabricate hollow carbon nanofibers uniformly coated with VNbC (VNbC/HMCFs) to mitigate self-stacking issues. To develop lithium-ion batteries with high energy densities, Fe_2MoC nanoparticles are grown in situ on VNbC/HMCFs via a hydrothermal process, forming the Fe_2MoC@VNbC/HMCFs composite electrode. The structure and morphology of the composite are characterized using scanning electron microscopy (SEM). As shown in Fig. S1(a_1), the VNbAlC MAX phase exhibits a characteristic layered structure. Following selective etching and exfoliation, a few-layer $VNbCT_x$ is obtained, as depicted in Fig. S1(a_2). Subsequently, coaxial electrospinning is employed to coat hollow carbon nanofibers with $VNbCT_x$, as

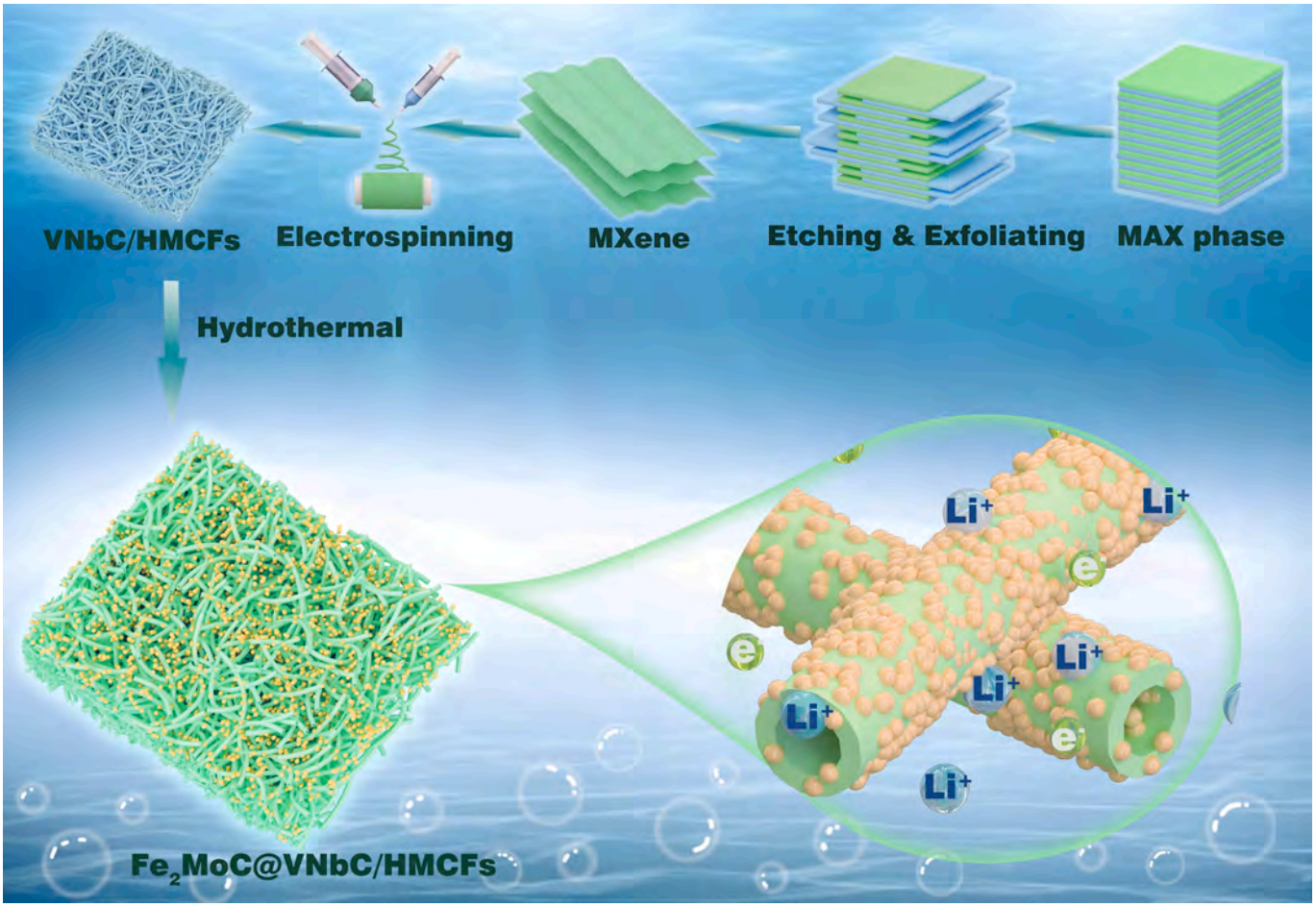

Fig. 1. Schematic diagram showing the synthesis of the Fe_2MoC@VNbC/HMCFs nanocomposite.

illustrated in Fig. S1(a_3). The fibers exhibit characteristic surface wrinkling, attributed to the uniform dispersion of $VNbCT_x$ nanosheets along the longitudinal axis of the PAN matrix without significant aggregation. This morphology confirms the exposure of abundant reactive edge sites on the $VNbCT_x$ nanosheets, thereby enhancing the availability of active sites [8]. Fe_2MoC nanoparticles are synthesized in situ on the hollow carbon nanofibers via a simple hydrothermal method, as shown in Fig. S1(b_{1-3}). The nanoparticles are uniformly anchored to both the inner and outer surfaces of the hollow structure, forming a continuous conductive network that facilitates efficient electron transport [9]. As shown in Fig. 2(a-c), Fe_2MoC@VNbC/HMCFs exhibit well-defined morphology, with the highly interconnected three-dimensional (3D) carbon nanofibers network serving as efficient pathways for rapid electron transport. Energy-dispersive X-ray spectroscopy (EDS) mapping (Fig. S2) confirms the uniform distribution of Fe, Mo, V, Nb, C, N, and O elements, validating the successful in situ formation of Fe_2MoC nanoparticles on the VNbC hollow carbon nanofiber matrix. (See Fig. 2.)

Transmission electron microscopy (TEM) reveals the internal architecture of both VNbC/HMCFs and Fe_2MoC@VNbC/HMCFs. As shown in Fig. 2(d), the VNbC/HMCFs display a well-defined hollow structure, offering internal void space to accommodate volume fluctuations during charge and discharge cycles. As shown in Fig. 2(e), the VNbC nanosheets are encapsulated within carbon nanofibers, exhibiting a lattice spacing of 0.15 nm [10]. The Fe_2MoC nanostructures are firmly anchored onto the hollow carbon nanofibers (Fig. 2(f)), effectively exposing numerous active sites and reducing ion diffusion pathways, thereby enhancing electrochemical performance. Chitosan, introduced during the hydrothermal reaction, serves as a carbon source for the formation of Fe_2MoC nanoparticles. During the subsequent carbonization process, these nanoparticles become encapsulated within a thin carbon layer, as illustrated in Fig. 2(g), further enhancing electrical conductivity and structural stability. The carbon coating on the active materials effectively safeguards the volume expansion of the Fe_2MoC nanoparticle array and $VNbCT_x$ nanosheets during lithium-ion insertion and extraction. This structural reinforcement prevents mechanical degradation, thereby minimizing capacity loss associated with material fracture and maintaining electrode integrity. As shown in Fig. 2(h), lattice spacings of 0.228 nm and 0.337 nm are observed, corresponding to the (340) plane of Fe_2MoC and the (002) plane of carbon, respectively [11]. The surface wettability of the composite is assessed by measuring the water contact angle, as presented in Fig. S3. The contact angle measured on Fe_2MoC@VNbC/HMCFs is smaller than that on VNbC/HMCFs and Fe_2MoC/HMCFs, indicating that the incorporation of hydrophilic VNbC MXene into the Fe_2MoC nanostructures enhances surface wettability and increases the electrode-electrolyte contact area [12]. A flexibility test was conducted to evaluate the mechanical flexibility of the self-supporting Fe_2MoC@VNbC/HMCFs electrode, as illustrated in Fig. S4.

XRD analysis reveals a peak at 24.7°, corresponding to the (002) plane of graphitic carbon, as shown in Fig. 2(i). The diffraction peaks associated with Fe_2MoC match well with the standard reference pattern (PDF 17–0911) [13]. The Raman spectra in Fig. S5(a) display broad peaks in the ranges of 1330–1400 cm^{-1} and 1587–1683 cm^{-1}, corresponding to the defect-induced D-band and the graphite-G-band, respectively. The D-band is attributed to sp^3 hybridized-disordered carbon structures, while the G-band corresponds to sp^2 hybridized graphitic carbon domains. Following the second carbonization step, the I_D/I_G ratio decreases from 1.06 to 0.38, indicating a significant transformation of the fiber structure toward graphitic carbon. This enhanced graphitization promotes improved electron transport within the Fe_2MoC@VNbC/HMCFs composite [14].

XPS is employed to analyze the chemical states of the elements in Fe_2MoC@VNbC/HMCFs. The full scan XPS spectrum shown in Fig. S5(b) confirms the presence of V, Nb, Fe, Mo, C, N, and O elements in the composite. In the XPS spectrum of Fe_2MoC@VNbC/HMCFs (Fig. S5(c)), the peaks at 515.4 and 522.1 eV correspond to V—C bonds and are attributed to the V $2p_{3/2}$ and V $2p_{1/2}$ orbitals, respectively. The additional peaks at 516.0 and 523.6 eV are assigned to $V^{4+,}$ while those at 516.9 and 524.9 eV are attributed to V^{5+}oxidation states [10]. The high-resolution XPS spectrum of the Nb region in Fig. S5(d) confirms the coexistence of Nb-O_x and Nb—C bonds. The peaks at 206.9 eV and 209.5 eV are attributed to Nb_2O_5, while the peaks at 203.8 eV and 206.3 eV correspond to Nb—C bonding. In the Fe 2*p* XPS spectrum (Fig. S5(e)),

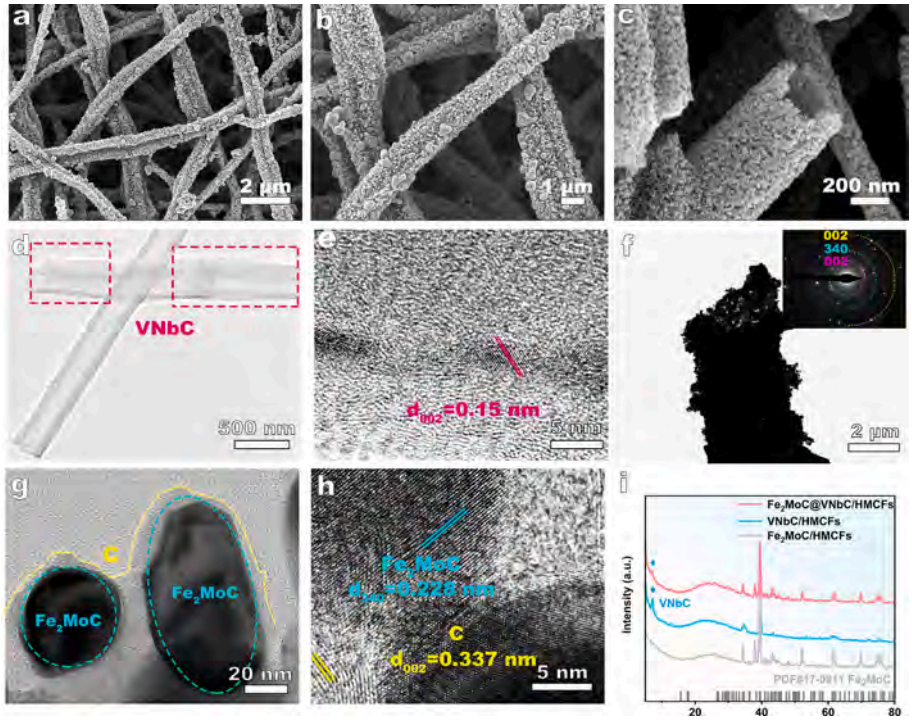

Fig. 2. (a-c) SEM images of Fe_2MoC@VNbC/HMCFs; (d) TEM image and (e) HR-TEM image of VNbC/HMCFs; (f, g) TEM images and (h) HR-TEM image of Fe_2MoC@VNbC/HMCFs; (i) XRD patterns of Fe_2MoC@VNbC/HMCFs, VNbC/HMCFs, and Fe_2MoC/HMCFs.

the peaks at 707.3 eV and 710.2 eV are assigned to Fe^{2+} $2p_{3/2}$ and Fe^{3+} $2p_{3/2}$, respectively, while the peaks at 722.9 eV and 725.3 eV correspond to Fe^{2+} $2p_{1/2}$ and Fe^{3+} $2p_{1/2}$, respectively [15–17]. The Mo 3*d* XPS spectrum in Fig. S5(f) can be deconvoluted into peaks corresponding to Mo 2*p* (228.4 eV and 231.8 eV), Mo 4*p* (230.1 and 235.5 eV), and Mo 6*p* (232.4 eV and 235.5 eV). The high-binding-energy peaks of Mo 4*p* and Mo 6*p* are attributed to surface oxidation of molybdenum, indicating the presence of high-valence Mo species [18,19]. The C 1 *s* XPS spectrum in Fig. S5(g) exhibits peaks at 281.8, 284.3, 284.8, 285.6, and 287.9 eV, which are assigned to C–V/Nb, C–Fe/Mo, C—C, C—O, and C=C=O, respectively [20,21]. Additionally, the incorporation of nitrogen during PAN pyrolysis enhances the density and electrical conductivity of the carbon nanofibers [22]. As shown in Fig. S5(h), the four peaks at 398.3 eV, 399.2 eV, 399.8 eV, and 400.9 eV correspond to N—O, pyridinic-N, pyrrolic-N, and graphitic-N species, respectively, confirming successful nitrogen doping within the carbonaceous framework [23]. The O 1 *s*

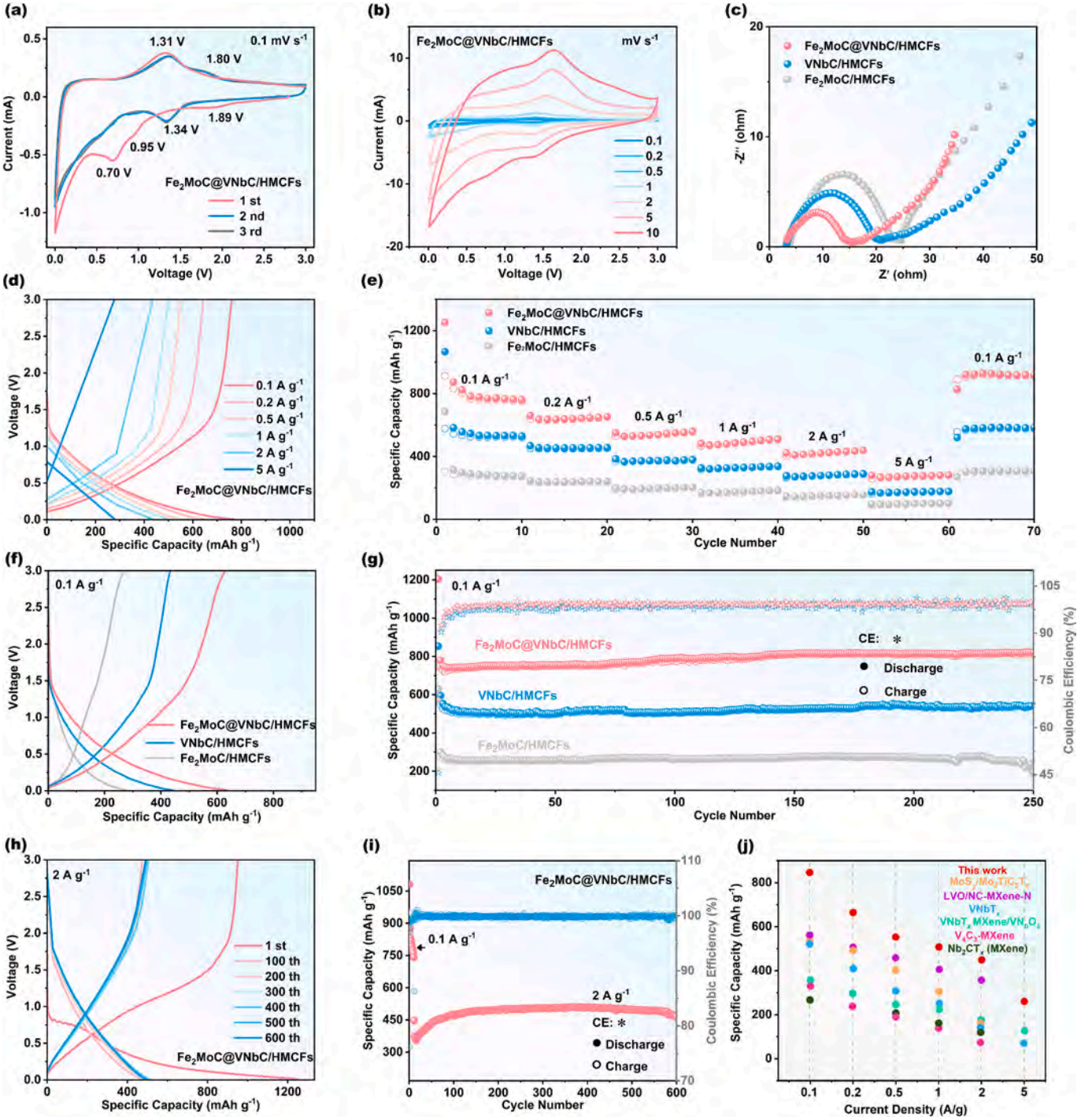

Fig. 3. (a) Cyclic voltammograms of the Fe_2MoC@VNbC/HMCFs electrode at a scan rate of 0.1 mV s^{-1}; (b) Cyclic voltammograms of Fe_2MoC@VNbC/HMCFs electrode at scan rates ranging from 0.1 mV s^{-1} to 10 mV s^{-1}; (c) Nyquist plots of Fe_2MoC@VNbC/HMCFs, VNbC/HMCFs, and Fe_2MoC/HMCFs electrodes; (d) Rate performance of Fe_2MoC@VNbC/HMCFs at various current densities; (e) Rate capabilities of Fe_2MoC@VNbC/HMCFs, VNbC/HMCFs, and VNbC/HMCFs; (f) Charge-discharge profiles and (g) Cycling performance of the Fe_2MoC@VNbC/HMCFs, VNbC/HMCFs, and Fe_2MoC/HMCFs electrodes at 0.1 A g^{-1}; (h) Charge-discharge profiles and (i) Cycling performance of Fe_2MoC@VNbC/HMCFs at a high current density of 2 A g^{-1}; (j) Comparison diagram.

spectrum in Fig. S5(i) displays distinct peaks corresponding to Nb_2O_5 (529.7 eV), O-V/Nb (530.7 eV), C—O (531.2 eV), and C═O (531.4 eV) [24,25]. confirming the presence of metal-oxygen and carbon-oxygen bonding environments.

To elucidate the electrochemical kinetics of Fe_2MoC@VNbC/HMCFs, the lithium storage mechanism is examined using cyclic voltammetry (CV). As shown in Fig. 3(a), the first three CV cycles of the Fe_2MoC@VNbC/HMCFs electrode are recorded at a scan rate of 0.1 mV s^{-1}. In the first cycle, the reduction peak at 0.70 V is attributed to the electrolyte decomposition and the formation of the solid-electrolyte interphase (SEI) [26]. The additional reduction peaks observed at 0.95 V and 1.89 V disappear in subsequent cycles, indicating their association with irreversible SEI formation processes [27]. The oxidation peak at 1.31 V is likely associated with Li^+ insertion/extraction within the VNbC interlayers, as well as surface adsorption/desorption processes [28]. The reduction peak at 1.34 V and the corresponding oxidation peak at 1.31 V constitute a redox pair, indicative of the reversible conversion reactions occurring on Fe_2MoC during charge-discharge cycling. Additionally, the peak observed at 1.80 V may also arise from similar conversion-related processes. The overlapping CV curves in the subsequent cycles indicate excellent electrochemical reversibility and stability of the Fe_2MoC@VNbC/HMCFs electrode [29]. For comparison, CV measurements were also performed on the VNbC/HMCFs and Fe_2MoC/HMCFs electrodes, as shown in Fig. S6(a, b). CV curves were recorded at various scan rates to further elucidate the lithium storage mechanism of Fe_2MoC@VNbC/HMCFs, as shown in Fig. 3(b). In addition, electrochemical impedance spectroscopy (EIS) was conducted to evaluate the conductivity and electrochemical kinetics of the electrodes, with the results presented in Fig. 3(c). The charge transfer resistance (R_{ct}) of Fe_2MoC@VNbC/HMCFs is measured at 11.6 Ω, which is significantly lower than that of VNbC/HMCFs (17.4 Ω) and Fe_2MoC/HMCFs (20.8 Ω). This reduction indicates that the incorporation of conductive VNbC enhances ion transport. At the same time, the distribution of Fe_2MoC nanostructures on both the inner and outer surfaces of the hollow carbon nanofibers shortens the lithium-ion diffusion path, together promoting more efficient Li^+ diffusion kinetics [30,31].

The rate capability and cycling performance of Fe_2MoC@VNbC/HMCFs were evaluated at room temperature to assess their potential for practical applications. As shown in Fig. 3(d), the galvanostatic charge-discharge at varying current densities of 0.1 to 5 A g^{-1} demonstrates the electrode's response under different operational conditions. With increasing current density, the charge-discharge curves remain well-overlapped, indicating minimal polarization and excellent electrochemical reversibility of the electrode. To further assess the electrochemical performance of the electrodes, the rate capability is presented in Fig. 3(e), which illustrates the specific capacities of the three samples across a range of current densities from 0.1 A g^{-1} to 5 A g^{-1}. As the current density increases, the reversible capacity of Fe_2MoC@VNbC/HMCFs gradually declines, which is characteristic of typical electrode behavior; however, the material maintains a stable and consistent capacity across the tested current range, indicating robust rate performance. Fe_2MoC@VNbC/HMCFs exhibit high specific capacities of 837.3, 645.6, 543.9, 489.5, 422.0, and 269.85 mAh g^{-1} at current densities of 0.1, 0.2, 0.5, 1, 2, and 5 A g^{-1}, respectively, demonstrating excellent capacity retention across a wide range of operating conditions. In contrast, VNbC/HMCFs deliver specific capacities of 553.4, 455.0, 375.4, 328.3, 278.5, and 171.1 mAh g^{-1} at current densities of 0.1, 0.2, 0.5, 1, 2, and 5 A g^{-1}, respectively, while Fe_2MoC/HMCFs exhibit lower capacities of 290.2, 238.5, 197.8, 174.7, 149.1, and 96.0 mAh g^{-1} under the same conditions. These results highlight the superior rate capability of Fe_2MoC@VNbC/HMCFs compared to the individual components. Upon returning the current density to 0.1 A g^{-1}, the Fe_2MoC@VNbC/HMCFs electrode exhibits a more rapid recovery of specific capacity compared to the other two electrodes, indicating superior structural stability and reversibility under high-rate cycling conditions [32,33]. Fig. 3(f) displays the charge-discharge cycling profiles of the Fe_2MoC@VNbC/HMCFs electrode, while Fig. 3(g) compares the cycling performance of all three electrodes at a current density of 0.1 A g^{-1}. During the first charge-discharge cycle, VNbC/HMCFs and Fe_2MoC/HMCFs exhibit initial discharge-specific capacities of 853.4 mAh g^{-1} and 631.0 mAh g^{-1}, respectively, with corresponding first cycle Coulombic efficiencies of 62.3 % and 46.6 %. The Fe_2MoC@VNbC/HMCFs electrode demonstrates a remarkably high initial discharge specific capacity of 1203.7 mAh g^{-1}, along with an improved first-cycle Coulombic efficiency of 69.8 %, indicating enhanced lithium storage capability and effective charge utilization. Fig. 3(h) presents the galvanostatic charge-discharge curves of Fe_2MoC@VNbC/HMCFs at a current density of 2 A g^{-1} over multiple cycles, exhibiting outstanding stability from the initial cycle through to the 600th cycle. After 600 charge-discharge cycles at a high current density of 2 A g^{-1}, the Fe_2MoC@VNbC/HMCFs electrode retains a high specific capacity of 471.6 mAh g^{-1}, highlighting its excellent cycling stability (Fig. 3(i)) [34,35]. The electrochemical performance is further benchmarked against recently reported analogous materials, as illustrated in Fig. 3(j) [36–41].

Motivated by the outstanding performance observed in the half-cell configuration, a full cell is assembled using the integrated Fe_2MoC@VNbC/HMCFs flexible electrode as the anode and commercial NCM811 as the cathode. As shown in Fig. 4(a), after 400 charge-discharge cycles at a current density of 0.1 A g^{-1}, the full cell retains a specific capacity of 158.7 mAh g^{-1}, corresponding to a capacity retention of 72.5 %. With increasing cycle number, the charge-discharge curves of the full cell maintain a consistent profile, as shown in Fig. 4(b), indicating stable electrochemical behavior. Furthermore, Fig. 4(c) demonstrates that the full cell exhibits good rate performance at current densities of 0.1, 0.2, 0.5, and 1 A g^{-1}, respectively.

To gain deeper insight into the electrochemical evolution of the Fe_2MoC@VNbC/HMCFs electrode in situ, XRD analysis was conducted during the first two cycles at a current density of 0.1 A g^{-1}. As shown in Fig. 5(a), the characteristic peak of Al at 44.7° is observed under the open-circuit voltage (OCV) conditions, which is attributed to the aluminum foil window of the in-situ XRD cell. During the first discharging cycle, the diffraction peak of Fe_2MoC at 38.3° gradually weakens and shifts toward higher angles, indicating lattice contraction due to lithium-ion insertion. Simultaneously, new peaks corresponding to FeMo at 39.9° and 47.2° (PDF 15–0539) progressively appear and intensify, confirming the occurrence of lithiation-induced phase transformation. As charging begins, Li ions begin to de-intercalate from the electrode structure, leading to a gradual weakening of the FeMo diffraction peaks due to the extraction of Li^+. During diffraction, the diffraction peak corresponding to Fe_2MoC becomes more pronounced, suggesting crystal growth likely driven by recrystallization processes following lithium extraction. Similar diffraction patterns were observed during the second charge/discharge cycle, indicating an almost fully reversible phase transformation. This confirms that redox reactions predominantly govern the lithium storage mechanism [42–44]. The corresponding 3D mountain plots (Fig. 5(b-d)), schematic of the discharging transformation reaction (Fig. 5(e)), and 2D isothermal contour plots (Figs. S7 and S8) collectively demonstrate that the diffraction peaks associated with Li^+ insertion/extraction and phase transformations can effectively track the structural evolution of the electrode during cycling [45].

To further evaluate the suitability of Fe_2MoC@VNbC/HMCFs as a lithium-ion battery anode, the role of the hollow carbon nanofiber architecture in accommodating the volume expansion induced by Li^+ insertion/extraction during charge-discharge cycles is investigated and compared with that of conventional solid carbon nanofibers (CNFs). After 300 charge-discharge cycles, SEM images reveal that the solid CNFs experience pronounced volume expansion, accompanied by the formation of thick SEI layers and subsequent rupture, indicating poor structural stability and interfacial degradation. This degradation can be attributed to the higher mechanical stress accumulated in solid carbon

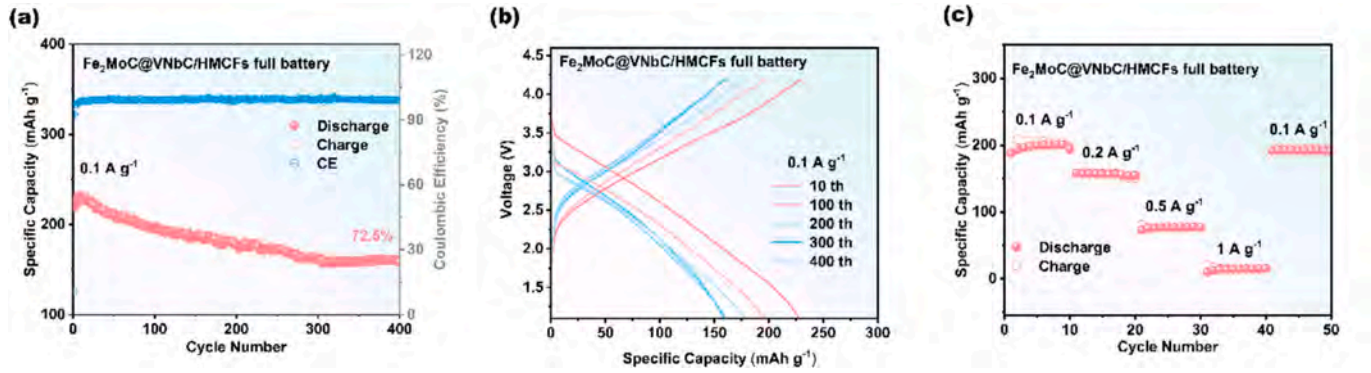

Fig. 4. (a) Cycling performance and (b) Charge-discharge curves of the Fe_2MoC@VNbC/HMCFs full battery at 0.1 A g^{-1}; (c) Rate capability of the Fe_2MoC@VNbC/HMCFs full battery.

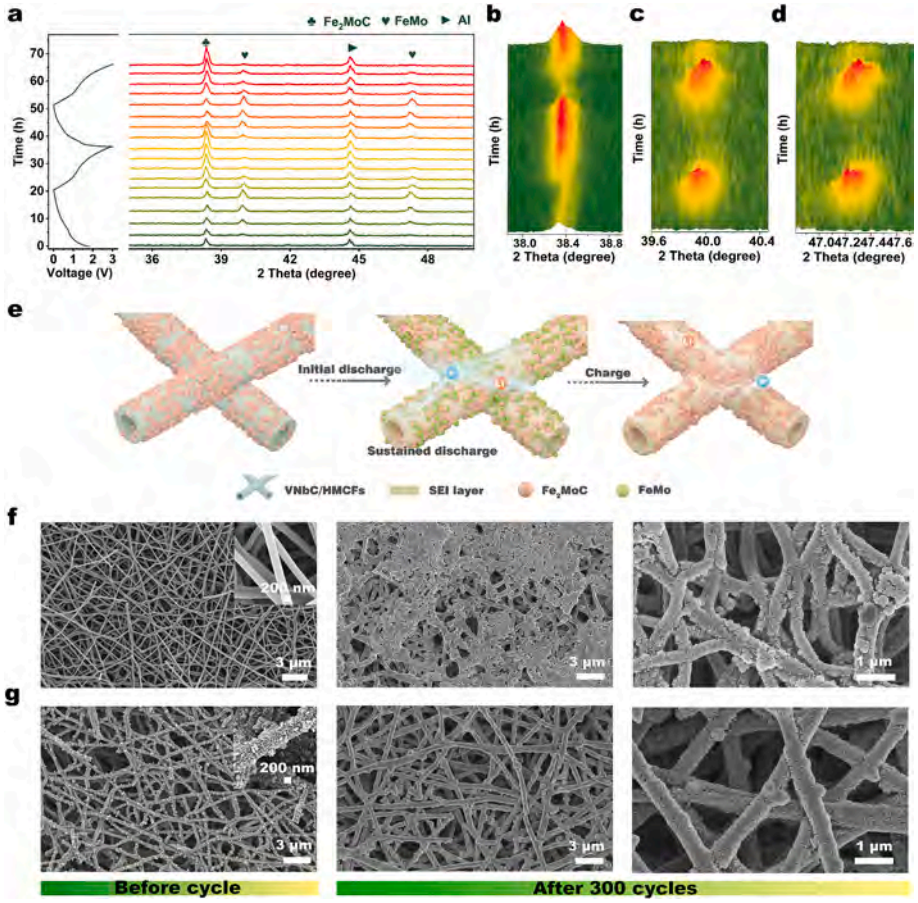

Fig. 5. (a) In situ XRD spectra at different charge-discharge states; (b-d) Mountain range maps showing the variation of typical XRD peaks over the first two cycles; (e) Schematic illustration of the conversion reaction of Fe_2MoC@VNbC/HMCFs during discharge; (f, g) SEM images of CNFs and Fe_2MoC@VNbC/HMCFs electrodes before and after cycling.

nanofibers during prolonged charge-discharge cycling, leading to structural fracture (Fig. 5(f)). Such damage compromises the electrode integrity, adversely affecting cycling stability and potentially causing a sharp decline in battery capacity. In contrast, the Fe_2MoC@VNbC/HMCFs electrode exhibits significantly reduced volume expansion and forms thinner SEI layers (Fig. 5(g)), while effectively preserving the structural integrity of the carbon nanofibers. Overall, these features contribute to the electrode's excellent electrochemical performance, highlighting its strong potential for application in high-performance lithium-ion batteries.

3. Conclusions

A novel hydrothermal synthesis approach is presented for fabricating Fe_2MoC nanoparticles embedded within VNbC-decorated hollow carbon nanofibers, tailored for application as high-performance anodes in lithium-ion batteries. By employing hollow carbon nanofibers as the substrate, the fiber confinement effect effectively prevents capacity degradation typically caused by the stacking and agglomeration of VNbC nanosheets and Fe_2MoC nanoparticles. Additionally, the hollow channels accommodate the volume fluctuations associated with Li^+ insertion and extraction, thereby enhancing structural stability and

improving the overall cycling performance of the lithium-ion battery. Benefiting from the synergistic integration of conductive VNbC MXene nanosheets and Fe_2MoC nanoparticle arrays, the electrode exhibits outstanding rate capability, delivering 269.85 mAh g^{-1} at a high current density of 5 A g^{-1}, along with excellent cycling stability, retaining a high specific capacity of 471.6 mAh g^{-1} after 600 charge-discharge cycles at 2 A g^{-1}. To demonstrate its commercial viability, the full cell achieves a capacity retention of 72.5 % after 400 cycles at a current density of 0.1 A g^{-1}. This study offers a new perspective on hierarchical electrode design and highlights the substantial potential of Fe_2MoC-based architectures for high-performance lithium-ion batteries.

CRediT authorship contribution statement

Xiaohong Lu: Writing – original draft, Data curation. **Yinghui Wang:** Formal analysis. **Weili Chen:** Data curation. **Wan Chang:** Methodology. **Deyang Zhang:** Methodology. **Kangwen Qiu:** Software. **Paul K. Chu:** Writing – review & editing. **Hailong Yan:** Formal analysis. **Jinbing Cheng:** Supervision.

Declaration of competing interest

The authors declare that they have no known competing financial interests or personal relationships that could have appeared to influence the work reported in this paper.

Acknowledgments

This work was financially supported by the National Natural Science Foundation of China (12305144 and 52401236), Natural Science Foundation of Henan Province (252300420063 and 242300420348), Key Scientific Research Projects of Higher Education Institutions in Henan Province (25A140006 and 24B140007), City University of Hong Kong Donation Research Grants (DON-RMG Nos. 9229021 and No. 9220061), as well as the Collaborative Innovation Center of Intelligent Explosion-proof Equipment of Henan Province.

Appendix A. Supplementary data

Supplementary data to this article can be found online at https://doi.org/10.1016/j.est.2025.117984.

Data availability

Data will be made available on request.

References

[1] Y. Zhou, W. Feng, Y. Xu, X. Liu, S. Wang, Z. Lv, X. Li, E. Burcar, Z. Wang, Z. Yang, A mechanical strategy of surface anchoring to enhance the electrochemical performance of ZnO/$NiCo_2O_4$@nickel foam self-supporting anode for lithium-ion batteries, Eng. Sci. 28 (2024) 1060.
[2] A. Huang, Y. Wu, H. Huang, C. Li, Y. Sun, L. Li, S. Peng, Lithiophilic Mo_2C clusters-embedded carbon nanofibers for high energy density lithium metal batteries, Adv. Funct. Mater. 33 (2023) 2303111.
[3] C. Zhang, W. Zhao, S.H. Park, T. Guo, S. Deng, A. Seral-Ascaso, M. Si, R. Grissa, S. Barwich, V. Nicolosi, Interconnected metallic membrane enabled by MXene inks toward high-rate anode and high-voltage cathode for Li-ion batteries, Adv. Funct. Mater. 33 (2023) 2213860.
[4] M. Tian, J. Lyu, R. Su, X. Zhang, K. Wang, X. Lv, D. Zhang, S.-W. Yang, J.H.K. Yip, Z. Hao, G.Q. Xu, Harnessing the power of nano-ferroelectrics: $BaTiO_3$/MXene ($Ti_3C_2T_x$) composites for enhanced lithium storage, Adv. Energy Mater. 14 (2024) 2401988.
[5] I. Pathak, D. Acharya, K. Chhetri, P.C. Lohani, T.H. Ko, A. Muthurasu, S. Subedi, T. Kim, S. Saidin, B. Dahal, H.Y. Kim, $Ti_3C_2T_x$ MXene integrated hollow carbon nanofibers with polypyrrole layers for MOF-derived freestanding electrodes of flexible asymmetric supercapacitors, Chem. Eng. J. 469 (2023) 14338.
[6] L. Li, Y. Ma, F. Cui, Y. Li, D. Yu, X. Lian, Y. Hu, H. Li, S. Peng, Novel insight into rechargeable aluminum batteries with promising selenium sulfide@carbon nanofibers cathode, Adv. Mater. 35 (2023) 2209628.
[7] Z. Wang, C. Wei, H. Jiang, Y. Zhang, K. Tian, Y. Li, X. Zhang, S. Xiong, C. Zhang, J. Feng, MXene-based current collectors for advanced rechargeable batteries, Adv. Mater. 36 (2023) 2306015.
[8] X. Lu, J. Cheng, D. Zhou, Y. Chen, H. Jiang, Y. Lu, D. Zhang, D. Kong, P.K. Chu, H. Y. Yang, Y. Luo, Highly flexible multilayer MXene hollow carbon nanofibers confined with Fe_3C particles for high-performance lithium-ion batteries, Chem. Eng. J. 478 (2023) 147366.
[9] Q. Lai, B. Yin, Y. Dou, Q. Zhang, Y. Zhu, Y. Yang, Electrospun carbon nanofiber-supported V_2O_3 with enriched oxygen vacancies as a free-standing high-rate anode for an all-vanadium-based full, Carbon Energy 6 (2024) e517.
[10] Y. Chen, Y. Huang, Q. Xu, L. Yang, N. Jiang, S. Yin, Vanadium niobium carbide ($VNbCT_x$) bimetallic MXene derived V_5S_8-Nb_2O_5@MXene heterostructures for efficiently boosting the adsorption and catalytic performance of lithium polysulfide, Mater. Horiz. 11 (2024) 6443–6454.
[11] X. Hao, J. Bi, W. Wang, W. Yan, X. Gao, X. Sun, R. Liu, Electrospun Fe_2MoC/C nanofibers as an efficient electrode material for high-performance supercapacitors, J. Power Sources 451 (2020) 227802.
[12] Y. Mei, J. Zhou, Y. Hao, X. Hu, J. Lin, Y. Huang, L. Li, C. Feng, F. Wu, R. Chen, High-lithiophilicity host with micro/nanostructured active sites based on Wenzel wetting model for dendrite-free lithium metal anodes, Adv. Funct. Mater. 31 (2021) 2106676.
[13] X. Hao, J. Bi, W. Wang, Y. Chen, X. Gao, X. Sun, J. Zhang, Bimetallic carbide Fe_2MoC as electrode material for high-performance capacitive energy storage, Ceram. Int. 44 (2018) 21874–21881.
[14] X. Hu, Y. Ma, W. Qu, J. Qian, Y. Li, Y. Chen, A. Zhou, H. Wang, F. Zhang, Z. Hu, Y. Huang, L. Li, F. Wu, R. Chen, Large interlayer distance and heteroatom-doping of graphite provide new insights into the dual-ion storage mechanism in dual-carbon batteries, Chen. Angew. Chem. Int. Edit. 62 (2023) e202307083.
[15] M. Han, J. Liu, C. Deng, J. Guo, Y. Mu, Z. Zou, K. Zheng, F. Yu, Q. Li, L. Wei, L. Zeng, T. Zhao, Yolk-Shell structure and spin-polarized surface capacitance enable FeS stable and fast ion transport in sodium-ion batteries, Adv. Energy Mater. 14 (2024) 2400246.
[16] H.W. Choi, H. Lee, J. Lu, S.B. Kwon, D.I. Jeong, B.J. Park, J. Kim, B.K. Kang, G. Jang, D.H. Yoon, H.S. Park, Trifunctional robust electrocatalysts based on 3D Fe/N-doped carbon nanocubes encapsulating Co_4N nanoparticles for efficient battery-powered water electrolyzers, Carbon Energy 6 (2024) e505.
[17] H. Liang, Z. Gai, F. Chen, S. Jing, W. Kan, B. Zhao, S. Yin, P. Tsiakaras, Fe_3C decorated wood-derived integral N-doped C cathode for rechargeable Li-O_2 batteries, Appl. Catal. B-Environ. 324 (2023) 122203.
[18] Z. Bayhan, J.K. El-Demellawi, J. Yin, Y. Khan, Y. Lei, E. Alhajji, Q. Wang, M. N. Hedhili, H.N. Alshareef, A laser-induced Mo_2CT_x MXene hybrid anode for high-performance Li-ion batteries, Small 19 (2023) 2208253.
[19] I. Jeon, L. Yin, D. Yang, H. Chen, S.W. Go, M.S. Kang, H.S. Ahn, C.-R. Cho, Enhanced Li storage of pure crystalline-C_{60} and $TiNb_2O_7$-nanostructure composite for Li-ion battery anodes, J. Energy Chem. 97 (2024) 478–485.
[20] Y. Huang, H. Gu, H. Zhang, X. Wang, L. Gao, Y. Cui, B. Zong, H. Li, W.-L. Dai, Synergistic V-Nb sites modulate selective alkene epoxidation with in situ photogenerated H_2O_2 over COF@MXene heterostructures, ACS Catal. 14 (2024) 12541–12550.
[21] L.-Y. Wang, C. Ma, J.-N. Yang, K.-X. Wang, J.-S. Chen, Organometallic polymer constructed by active Fe-$C_{12}N_8$ centers for boosting sodium-ion storage, Angew. Chem. Int. Ed. 64 (2025) e202413452.
[22] H. Jo, J.H. Park, D. Choi, K. Kim, S. An, Percolative metal microweb-based flexible lithium-ion battery with fast charging and high energy density, Adv. Mater. 2407719 (2024).
[23] Y. Guo, D. Zhang, Z. Bai, Y. Yang, Y. Wang, J. Cheng, P.K. Chu, Y. Luo, MXene nanofibers confining MnO_x nanoparticles: a flexible anode for high-speed lithium-ion storage networks, Dalton Trans. 51 (2022) 1423–1433.
[24] Y. Liu, W. Zhong, C. Yang, X. Liu, Q. Cheng, T. Tan, Q. Deng, C. Yang, Defective state regulation of Ru-doped Nb_2O_5 boosts fast lithium storage, J. Colloid. Interf. Sci. 667 (2024) 136–146.
[25] Z. Bai, D. Zhang, Y. Guo, Y. Yang, H. Yan, Y. Wang, J. Cheng, P.K. Chu, H. Pang, Y. Luo, Hierarchical cobalt-nickel double hydroxide arrays assembled on naturally Sedimented $Ti_3C_2T_x$ for high-erformance flexible supercapacitors, Adv. Sustain. Syst. 6 (2022) 2100371.
[26] A.A. AbdelHamid, A. Mendoza-Garcia, S.S. Lee, J.Y. Ying, Metal oxide- and metal-loaded mesoporous carbon for practical high-performance Li-ion battery anodes, Nano Energy 119 (2024) 109025.
[27] D. Lan, Y. Gu, X. Chen, M. Mo, Z. Fang, P. Xiong, W. Ye, G. Zhao, T. Xiong, M. Huang, W. Li, H. Zhan, X. Ming, G. Huang, G. Li, F. Zhan, Quasi-closed-loop approach for facile and environmentally friendly red mud reutilization as advanced Li-ion anode material, J. Clean. Prod. 439 (2024) 140680.
[28] L. Lu, G. Guan, J. Wang, W. Meng, S. Li, Y. Zhang, F. Guo, Nitrogen-doped carbon dots modified double transition metal MXene ($Ti_2NbC_2T_x$) for superior lithium/sodium-ion storage, Chem. Eng. J. 480 (2024) 147999.
[29] J. Cheng, X. Lu, D. Zhang, H. Yan, C. Liu, J. He, C. Zheng, H. Shi, P.K. Chu, Y. Luo, N-doped hollow multichannel carbon nanofibers encased in Fe_3C for lithium-ion storage, ACS Appl. Nano Mater. 7 (2024) 10543–10551.
[30] F. Xie, L. Zhang, C. Ye, M. Jaroniec, S.-Z. Qiao, The application of hollow structured anodes for sodium-ion batteries: from simple to complex systems, Adv. Mater. 31 (2019) 1800492.
[31] Z. Chen, X. Lu, Y. Zhang, Y. Kang, X. Jin, X. Zhang, Y. Li, H. Wang, W. Huang, Ultra-low 4.3 wt% silicon thermal reducing doped porous Si@MoC as highly capable and stable Li-ion battery anode, Adv. Funct. Mater. 34 (2024) 2314176.
[32] X. Yang, M. Gong, Z. Liu, C. Huangfu, Y. Yan, C. Chi, Y. Lin, B. Qi, G. Wang, K. Cao, X. Li, T. Wei, Z. Fan, Multi-dimensional assembly of ZnO nanodots in the reticular

carbon nanofibers for high-performance lithium-ion batteries, Carbon 223 (2024) 119001.
[33] J. Cao, Y. Shi, A. Gao, G. Du, M. Dilxat, Y. Zhang, M. Cai, G. Qian, X. Lu, F. Xie, Y. Sun, X. Lu, Hierarchical Li electrochemistry using alloy-type anode for high-energy-density Li metal batteries, Nat. Commun. 15 (2024) 1354.
[34] F. Liang, H. Dong, J. Dai, H. He, W. Zhang, S. Chen, D. Lv, H. Liu, I.S. Kim, Y. Lai, Y. Tang, M. Ge, Fast energy storage of SnS_2 anode nanoconfined in hollow porous carbon nanofibers for lithium-ion batteries, Adv. Sci. 11 (2024) 2306711.
[35] Z. Long, H. Dai, C. Wu, Z. Li, H. Qiao, K. Wang, Q. Wei, Growth-controllable spindle chain heterostructural anodes based on MIL-88A for enhanced Lithium/sodium storage, Adv. Fiber Mater. 6 (2024) 297–311.
[36] A. Byeon, A.M. Glushenkov, B. Anasori, P. Urbankowski, J. Li, B.W. Byles, B. Blake, K.L. Van Aken, S. Kota, E. Pomerantseva, J.W. Lee, Y. Chen, Y. Gogotsi, Lithium-ion capacitors with 2D Nb_2CT_x (MXene)-carbon nanotube electrodes, J. Power Sources 326 (2016) 686–694.
[37] J. Zhou, S. Lin, Y. Huang, P. Tong, B. Zhao, X. Zhu, Y. Sun, Synthesis and lithium ion storage performance of two-dimensional V_4C_3 MXene, Chem. Eng. J. 373 (2019) 203–212.
[38] C. Xu, K. Feng, X. Yang, Y. Cheng, X. Zhao, L. Yang, S. Yin, In-situ construction of metallic oxide ($VNbO_5$) on $VNbCT_x$ MXene for enhanced Li-ion batteries performance, J. Power Sources 69 (2023) 107888.
[39] Y. Cheng, L. Yang, S. Yin, Synthesis and lithium ion storage performance of novel two dimensional vanadium niobium carbide ($VNbCT_x$) MXene, Compos. Commun. 40 (2023) 101588.
[40] C. Chen, X. Xie, B. Anasori, A. Sarycheva, T. Makaryan, M. Zhao, P. Urbankowski, L. Miao, J. Jiang, Y. Gogotsi, MoS_2-on-MXene Heterostructures as highly reversible anode materials for Lithium-ion batteries, Angew. Chem. Int. Ed. 57 (2018) 1846–1850.
[41] S. Yang, D. Zhang, J. Xu, Z. Zhang, S. Ni, Robust pseudocapacitive charge storage behavior in Li_3VO_4 induced by N doped MXene, Electrochim. Acta 388 (2021) 138567.
[42] S. Guo, Z. Sun, Y. Liu, X. Guo, H. Feng, S. Luo, C. Wei, Y. Zheng, X. Zhang, K. Kim, H. Liu, P.K. Chu, B. Gao, Q. Zhang, K. Huo, Multiscale micro-nano hierarchical porous germanium with self-adaptive stress dispersion for highly robust lithium-ion batteries anode, Adv. Energy Mater. 14 (2024) 2303876.
[43] Y. Liu, W. Guan, S. Li, J. Bi, X. Hu, Z. Du, H. Du, W. Ai, W. Huang, Sustainable dual-layered interface for long-lasting stabilization of lithium metal anodes, Adv. Energy Mater. 13 (2023) 2302695.
[44] W. Yu, B. Cui, J. Han, S. Zhu, X. Xu, J. Tan, Q. Xu, Y. Min, Y. Peng, H. Liu, Y. Wang, In situ encapsulation of SnS_2/MoS_2 heterojunctions by amphiphilic graphene for high-energy and ultrastable lithium-ion anodes, Adv. Sci. 11 (2024) 2405135.
[45] S. Zhu, W. Nong, L.J.J. Nicholas, X. Cao, P. Zhang, Y. Lu, M. Xiu, K. Huang, G. Wu, S.-W. Yang, J. Wu, Z. Liu, M. Srinivasan, K. Hippalgaonkar, Y. Huang, Rapid in situ growth of high-entropy oxide nanoparticles with reversible spinel structures for efficient Li storage, J Mater Chem A 12 (2024) 11473–11486.

Supporting Information

In situ construction of Fe_2MoC nanostructures on VNbC MXene carbon nanofibers for enhanced lithium-ion battery performance

Xiaohong Lu [a], Yinghui Wang [a,*], Weili Chen [a], Wan Chang [a,*], Deyang Zhang [b], Kangwen Qiu [c], Paul K. Chu [d], Hailong Yan [a], Jinbing Cheng [a,*]

[a] Henan International Joint Laboratory of MXene Materials Microstructure, College of Physics and Electronic Engineering, Nanyang Normal University, Nanyang 473061, China

[b] Key Laboratory of Microelectronics and Energy of Henan Province, Xinyang Normal University, Xinyang 464000, China

[c] College of Energy Engineering, Huanghuai University, Zhumadian 463000, China

[d] Department of Physics, Department of Materials Science & Engineering, and Department of Biomedical Engineering, City University of Hong Kong, Tat Chee Avenue, Kowloon, Hong Kong, China

*Corresponding authors: yhsewang@163.com (Y. Wang); changwan@nynu.edu.cn (W. Chang); chengjinbing1988@163.com (J. Cheng)

1. Materials

Polyacrylonitrile (PAN, Mw = 250,000) was purchased from Macklin and polymethyl methacrylate was provided by LG company. Ferric chloride tetrachloride ($FeCl_2 \cdot 4H_2O$, 99%), Ammonium molybdate tetrahydrate ($(NH_4)_6Mo_7O_{24} \cdot 4H_2O$, 99.9%), cetyltrimethylammonium bromide (CATB, 99%), and chitosan were bought from Innochem. VNbAlC was purchased from (Suzhou Beike Nano Co., Ltd), and N, N-dimethylformamide (DMF, 99.5%) was supplied by Aladdin. All the reagents were analytical grade and used without further purification.

2. Preparation of $VNbCT_x$ MXene

Add lithium fluoride (1 g) to 30 mL of 9 mol/L hydrochloric acid, stir for 5 minutes, then add 40% hydrofluoric acid (5 mL) and stir for 15 minutes. Subsequently, add VNbAlC in several portions over a period of one and a half hours. To prevent VNbAlC from oxidizing due to excessive temperature, the mixture was kept below 40 °C and stirred for 48 hours. Hydrofluoric acid etched the Al layer from VNbAlC. Then, the solution was centrifuged at 5000 rpm until it became a suspension. The obtained $VNbCT_x$ MXene solution was transferred to a bottle, ultrasonically treated at low temperature for 1 hour, and then placed under argon for 1 hour. In the electrospinning experiment, the sample was centrifuged with dimethylformamide (DMF) at 40 °C and at 10000 rpm for 1.2 hours. This process was repeated twice to obtain the $VNbCT_x$ MXene solution. During this process, the temperature should be kept below 40 °C to prevent the oxidation of $VNbCT_x$ MXene nanosheets.

3. Preparation of VNbC/HMCFs

The VNbC MXene flakes and N, N-dimethylformamide were ultrasonically dispersed in ice water, and polypropylene was added and stirred to form solution a. Poly (methyl methacrylate) was added to N, N-dimethylformamide, and the homogeneous inner layer solution obtained after stirring was designated as solution b. Separate syringes were filled with the inner and outer layer solutions for coaxial spinning. The flow rates of the core and shell solutions were 0.22 and 0.5mL h^{-1}, respectively. The distance between the spinneret and the receiving roller was 13 cm, and the voltage was 27 kV. Finally, the nanofibers were dewatered at a temperature of 60 ℃ in air for 6 h, annealed at 250 °C for 125 minutes (2 °C min^{-1}) under air, and carbonized at 700 ℃ for 70 minutes (7 °C min^{-1}) under argon gas to obtain VNbC/HMCFs.

4. Preparation of Fe_2MoC@VNbC/HMCFs

Cetyltrimethylammonium bromide (CTAB) (1 g) was dissolved in 40 mL of deionized water and stirred for 0.5 h to form solution a. Chitosan (0.9 g) was dissolved in 40 mL of deionized water to form solution b. Solutions a and b were mixed to form solution c, to which 0.6 g of $FeCl_2 \cdot 4H_2O$ and 0.8 g of $(NH_4)_6Mo_7O_{24} \cdot 4H_2O$ were added successively and stirred. VNbC/HMCFs were added, transferred to a reactor heated to 200 ℃ for 12 hours, and washed with deionized water and anhydrous ethanol repeatedly. After heating under argon gas to 850 ℃ for 1.5 hours, Fe_2MoC@VNbC/HMCFs were obtained.

5. Characterization

The structure and phases were determined by X-ray diffraction (XRD, Rigaku D/Texultra 250) in the 2-theta angle range of 5°-80° using a Cu K_α source. Raman scattering was conducted on the Renishaw microprobe with a 532 nm laser and a 50x objective lens. The chemical composition and functional groups were investigated by X-ray photoelectron spectroscopy (XPS, K-ALPHA with a resolution of 0.5 eV, Thermo Scientific, USA). The morphology and structure of the samples were examined by field-emission scanning electron microscopy (FE-SEM, Gemini-SEM 300, ZEISS, Germany) and transmission electron microscopy (TEM, Talos F200x instrument (FEI, USA). Elemental analysis was performed by energy-dispersive X-ray spectroscopy (Bruker-QUANTAX).

6. Electrochemical evaluation

The Fe_2MoC@VNbC/HMCFs, Fe_2MoC/HMCFs, and VNbC/HMCFs were sectioned into small discs with a diameter of approximately 16 mm to form the anodes without additives. The standard 2032-type coin cells were assembled in an argon-filled glove box. The electrolyte was 1 M $LiPF_6$ in mixed DOL (1, 3-dioxolane) and DME (1, 2-dimethoxyethane) with a volume ratio of 1:1. Galvanostatic charging-discharging, cycling, and rate capacity tests were conducted on the LANDIAN CT3001A. Cyclic voltammetry (CV) was carried out between 0.01 and 3.0 V, and electrochemical impedance spectroscopy (EIS) was performed on an electrochemical workstation (PGSTAT302N).

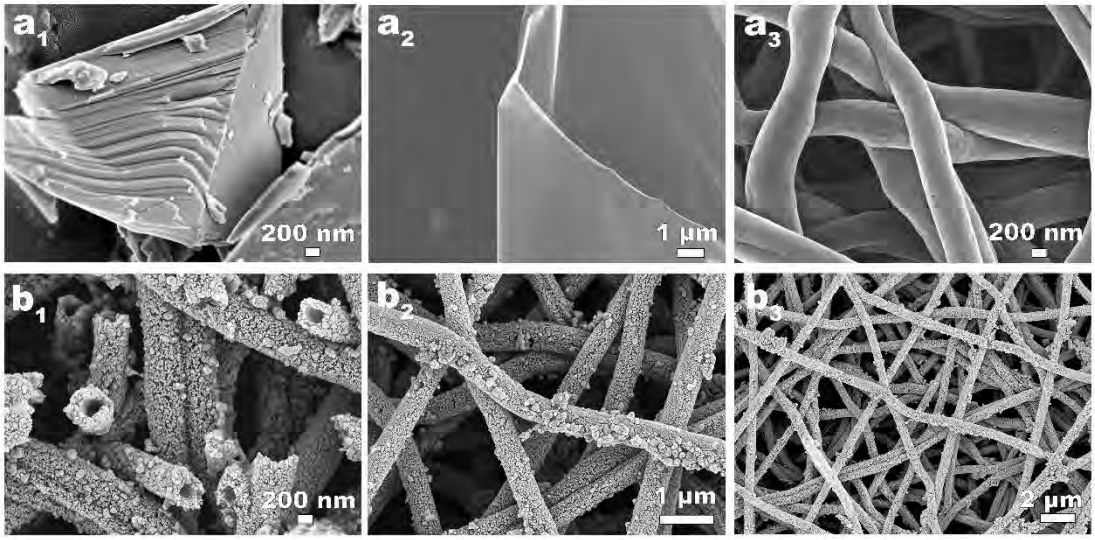

Fig. S1. (a_1) SEM image of VNbAlC, (a_2) SEM image of VNbC nanosheets, (a_3) SEM image of VNbC/HMCFs, and (b_1-b_3) SEM images of Fe_2MoC/HMCFs.

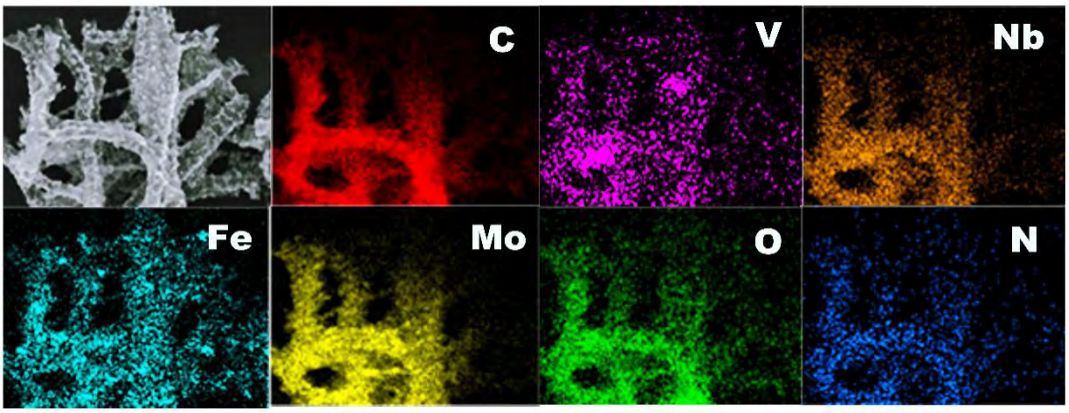

Fig. S2. EDS elemental mapping images of Fe_2MoC@VNbC/HMCFs.

Fig. S3. Water contact angles on Fe_2MoC@VNbC/HMCFs, VNbC/HMCFs, and Fe_2MoC/HMCFs.

Fig. S4. Photographs of the flexible Fe_2MoC@VNbC/HMCFs film.

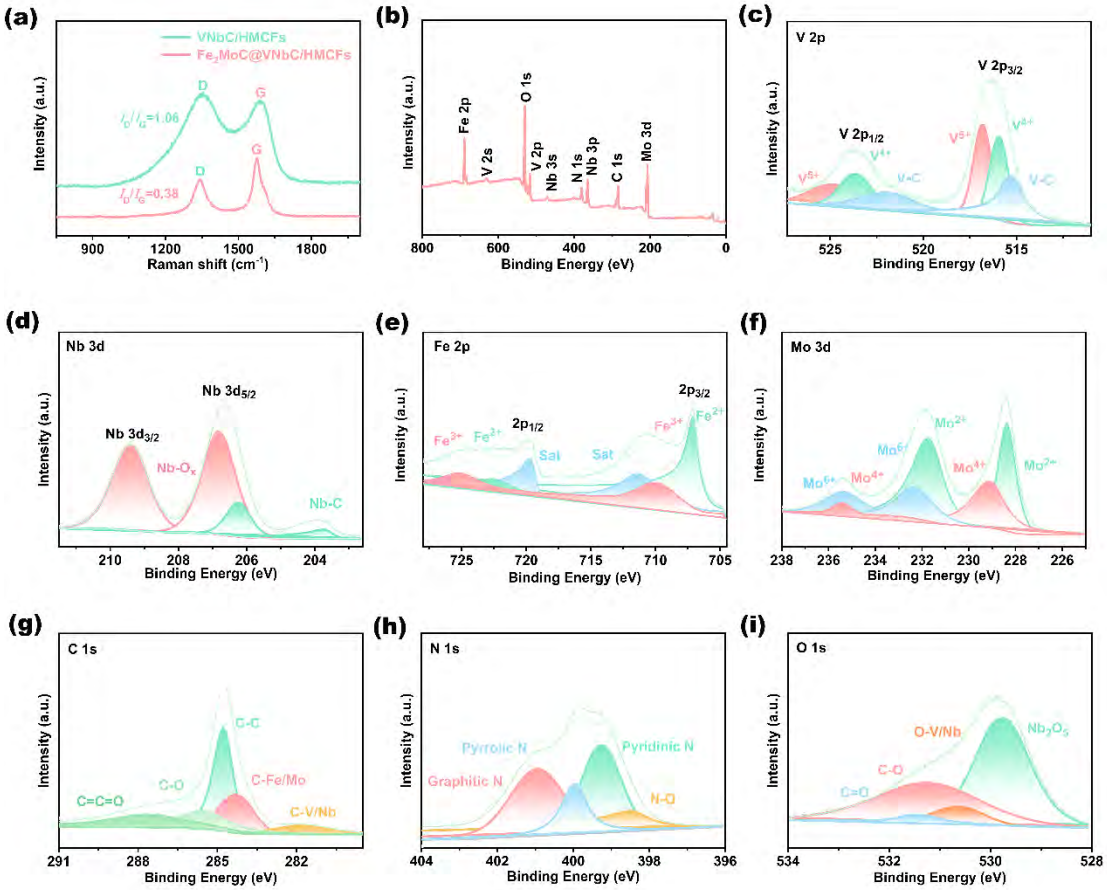

Fig. S5. (a) Raman scattering spectra of Fe_2MoC@VNbC/HMCFs and VNbC/HMCFs; (b) Survey and (c) V 2*p*, (d) Nb 3*d*, (e) Fe 2*p*, (f) Mo 3*d*, (g) C 1*s*, (h) N 1*s*, and (i) O 1*s* XPS spectra of Fe_2MoC@VNbC/HMCFs.

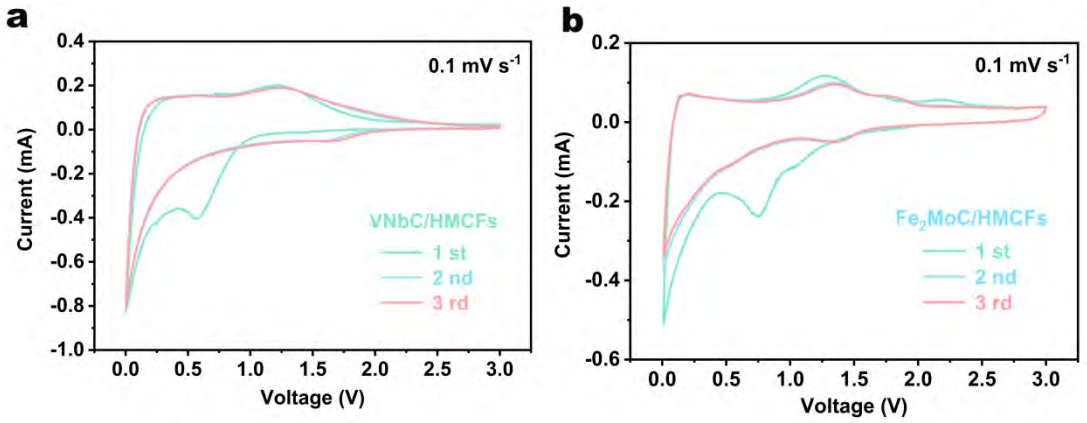

Fig. S6. (a) Cyclic voltammograms of the VNbC/HMCFs electrode at a scanning rate of 0.1 mV s^{-1} and (b) Cyclic voltammograms of the Fe_2MoC/HMCFs electrode at a scanning rate of 0.1 mV s^{-1}.

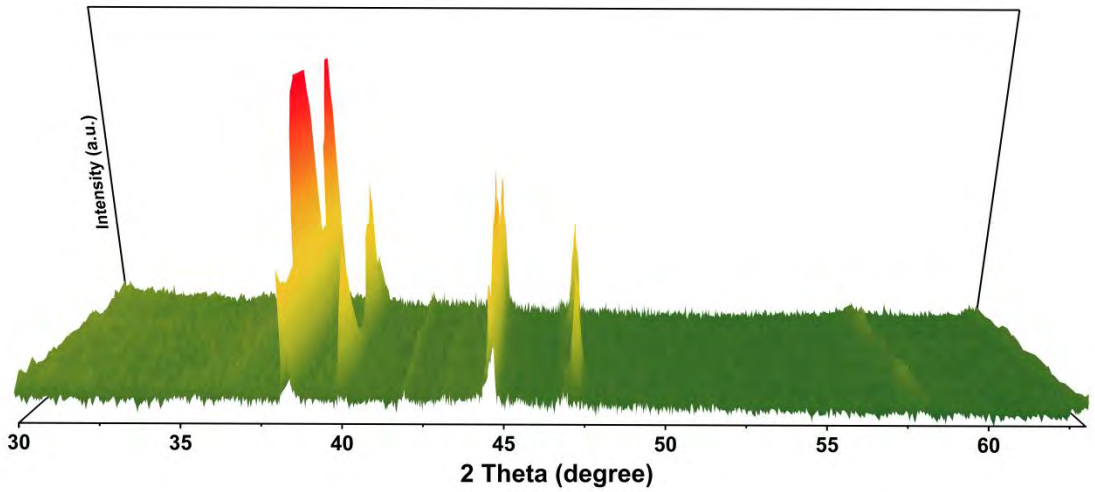

Fig. S7. In situ XRD spectra of Fe_2MoC@VNbC/HMCFs during lithiation/delithiation.

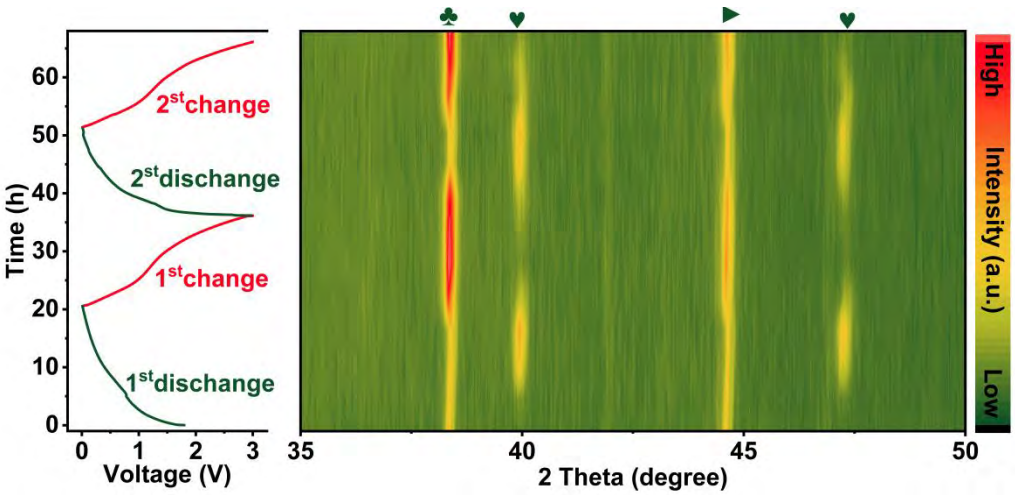

Fig. S8. In situ XRD results for different discharging/charging cycles and contour plots of the initial two cycles.